



Failure mode diagnosis in proton exchange membrane fuel cells using local electrochemical noise

M.A. Rubio ^{a,*}, D.G. Sanchez ^b, P. Gazdzicki ^b, K.A. Friedrich ^{b,c}, A. Urquia ^a

^a Dept. Informática y Automática, Universidad Nacional de Educación a Distancia (UNED), 28040 Madrid, Spain

^b Institute of Engineering Thermodynamics, Deutsches Zentrum für Luft und Raumfahrt (DLR), 70569 Stuttgart, Germany

^c Institute of Building Energetics, Thermal Engineering and Energy Storage (IGTE), University of Stuttgart, 70569 Stuttgart, Germany

HIGHLIGHTS

- The method allows the cell in operation using lightweight, and inexpensive device.
- Local electrochemical noise analyzed to diagnose fault modes.
- Classification of faults carries out successfully through a deep learning network.

ARTICLE INFO

Keywords:

PEM fuel cell
Local diagnosis
Electrochemical noise
Wavelet transform
Neural networks

ABSTRACT

Early diagnosis of fuel cell failure modes is a very active research topic, as it improves robustness and durability of fuel cells used in commercial applications. The diagnosis method should be suited for being applied in real time, without interfering with the fuel cell operation, and it should be implemented using inexpensive hardware and light equipment. A novel method of failure diagnosis in PEM fuel cells, based on the analysis of local electrochemical noise, is proposed. Seven electrochemical noise signals are acquired in different parts of the cell, significantly increasing the information for an effective diagnosis, since previous studies have only analyzed a single signal from the electrochemical noise in the cell.

Each electrochemical noise signal is frequency decomposed using wavelet transform to create a characteristic pattern. These patterns are used in a deep learning neural network to perform the cell state classification. The proposed method has been successfully applied to the classification of 26 different states achieved in experiments where the following factors have been varied: (1) average current density; (2) airflow; (3) drying; and (4) air pressure. The mean successful identification rate of the 26 states is above 85%. The proposed diagnosis method is well-suited for real-time diagnosis, and it can be implemented using lightweight and inexpensive hardware.

1. Introduction

In the current economic and environmental situation, the sustainable use of energy is a key factor for the development of our society. Fuel cells and specifically proton exchange membrane fuel cells (PEMFC), are one of the most promising devices as portable power generation systems. In transport applications, PEMFC are an alternative to internal combustion engines, and they are considered as a technology to reduce greenhouse gas emissions.

The extent of PEMFC usage at the commercial level depends significantly on the efficiency and robustness of the PEMFC operation [1]. Due to the complexity of these electrochemical devices, early detection of PEMFC failure modes plays an important role in improving their

efficiency and robustness, since it may prevent or mitigate the fault-induced damages, reducing maintenance costs. Premature diagnosis of failures, while these have not caused any irreversible damage to the cell yet, allows restoring optimal operating conditions.

Two desirable features of an early diagnosis method, to be well suited for its implementation in commercial portable PEMFC systems, are the following. Firstly, the diagnosis process should be performed in real-time on the operating cell, without influencing or interfering with the normal operation of the cell. Secondly, the diagnosis system should be made using lightweight, non-voluminous and inexpensive hardware.

Various methods have been proposed for in-situ identification of operating and failure modes.

* Corresponding author.

E-mail address: marubio@dia.uned.es (M.A. Rubio).

<https://doi.org/10.1016/j.jpowsour.2022.231582>

Received 11 November 2021; Received in revised form 1 May 2022; Accepted 4 May 2022

Available online 1 June 2022

0378-7753/© 2022 The Author(s). Published by Elsevier B.V. This is an open access article under the CC BY-NC-ND license (<http://creativecommons.org/licenses/by-nc-nd/4.0/>).

EIS diagnosis is used to analyze the frequency response of the cell impedance, produced by the injection of electrical signals. The faults due to air compressor, fuel poisoning, and stack overheating are classified using EIS data [2]. The impedance of the electrochemical device is studied as a transfer function using EIS measurements in [3]. Also, EIS data are applied to analyze the effect in the PEMFC of methanol in freeze cycles [4], and to compare the internal resistance of different degradation phenomena [5]. The scaling-up technique and Buckingham's Pi theorem are used in the estimation of stack PEMFC impedance [6,7].

The current interruption method analyzes the electrical response of the cell due to abrupt current interruptions. In particular, the analysis of the voltage response allows to calculate some electrochemical parameters [8] and the ohmic resistance of the cell [9]. Fault diagnosis through analysis of current local distribution in the cell using segmented cells has been studied. A real-time local current of PEMFC is calculated in [10] for different number of segmented cells. The effect of CO poisoning [11] and acetylene [12] using current and EIS local distribution are analyzed using segmented cells in PEMFC. Some current measurement methods of current local densities are studied in [13]. The spatial degradation due to load cycling has been evaluated in PEMFC [14].

The concentration-alternating frequency response analysis (cFRA) method, which modifies the oxygen concentration, allows to analyze cell humidification problems. The study of amplitude rate and phase differences between voltage and pressure oscillation is proposed as a diagnosis method of operating conditions of PEMFC cathode in [15]. The PEMFC's cathode humidification state is diagnosed using cFRA [16].

The galvanostatic charge method is used in [17] to analyze fuel cell degradation processes. Kalman filtering [18] is used to estimate the cell degradation processes and predict the lifetime from polarization curve fitting. Voltage analysis of a fuel cell stack, using the support vector machine (SVM), is applied to perform the diagnosis of 4 operating failures [19], and up to 5 failures simultaneously in stacks of different size [20]. Also, SVM and K-Nearest Neighbors (KNN) are combined to classify 6 different faults using the voltage frequency spectrum [21].

A hybrid method, combining machine learning, adaptive neuro-fuzzy inference system, and unscented Kalman filter algorithm is used to evaluate the useful life of PEMFC in [22]. Neural networks (NN) and model-based fault detection are used to identify the flooding, and membrane drying of PEMFC [23]. Also, a model-based diagnosis is applied to identify faults in automotive PEMFC systems [24]. Deep learning network (DLN) is a type of NN very effective in problems with a large number of input parameters, as this network allows to discriminate the most sensitive parameters from those parameters that do not provide useful information for classification. DLN is used in [25] to identify 10 failure modes of solid oxide fuel cells. Also, it is used to predict the speed of a fuel cell vehicle to allow proper regulation of oxygen stoichiometry [26].

The electrochemical noise (EN) has been employed in the study of several electrochemical processes and devices, such as corrosion processes [27–30], coatings [31–33] and batteries [34–37]. The use of EN in fuel cell analysis is more recent. The EN is applied in glucose biofuel cells [38]. The statistical correlation of EN is used for flooding diagnosis [39] and the EN is classified based on the building of hierarchical structures in [40]. The spectral power densities of the EN are analyzed, dividing into three frequency bands [41].

The theory about the nature of EN in fuel cells is still under discussion, being an active research area. Regardless of the relationship between the EN and the physical phenomena that produce it, the EN introduces an oscillation into the cell voltage signal in the low frequency band (1 Hz–1000 Hz), modulated by the cell electrical impedance [42–44].

The full frequency spectrum of the EN signal has been analyzed in [41,45], adjusting the spectrogram as is similarly done in corrosion process analysis. The EN variance has also been studied to diagnose different stages in the flooding process [46]. The frequency response

of EN patterns has been analyzed using wavelet transform [47,48] for different operational and failure modes.

The fuel cell EN is analyzed in some studies using artificial neural networks, due to EN signals' complexity. NN are a type of machine learning algorithm useful in pattern identification, and widely used in many fields of science. They are applied to identify EN frequency patterns in [48,49].

The systems previously described are very useful for the diagnosis and study of PEM cells in the laboratory. However, the EN analysis method solves the weight and price problems of other methods, making it a suitable option for use in autonomous portable commercial systems.

In this paper, we propose a novel method of fault diagnosis, and identification of operating modes, based on the analysis of local EN using wavelet transform (WT). Voltage fluctuations in different areas of the cell are measured and analyzed, obtaining richer information than in other studies where only the overall EN of the cell is considered. DLN algorithms are applied to classify the patterns associated to the different operating and failure modes. The use of DLN algorithms is justified by the massive amount of data that is contained in each pattern and needs to be analyzed.

To illustrate the capability of the proposed method, the identification of 26 different cell states is discussed. These 26 states are achieved in four groups of experiments, where the following quantities are varied respectively: (1) average current density; (2) airflow, ranging from typical operating conditions to starvation values; (3) cell hydration, including severe dehydration conditions; and (4) air pressure. The experimental setup is described in the next section.

2. Experimental setup

All experiments have been carried out in the DLR laboratories, using a home-made test bench with PLC control that allows automatic control of operational conditions (i.e., pressure, temperature, flow rate of gases, and reactants' humidity).

The local current density distribution is monitored using DLR's printed circuit board (PCB) [50,51]. The segmented PCB (divided into 7×7 matrix of segments) is integrated with the anode side's flow field. The same segmented cell configuration is used to obtain the local EN measurements, as shown in Fig. 1, using the seven central segments. The segments selected for measuring EN show behavioral differences for each cell operating mode, giving relevant information that can be useful to identify modes that have a variation of some of their variables in the gas inlet–outlet direction. The cell used in the experiments has a serpentine channel configuration, with three parallel channels. The anode and cathode have a co-flow configuration, as can be seen in Fig. 1. The cells used in the experiments have a commercial GORE catalyst coated membrane and a GDL Sigratec 25BC. The cell has a total surface of $0.25 \cdot 10^{-4} \text{ m}^2$ (25 cm²). The baseline of the experimental configuration is $1 \cdot 10^4 \text{ A m}^{-2}$ (1 A cm⁻²) of electric average current density in galvanostatic mode, $2.75 \cdot 10^{-5} \text{ m}^3 \text{ s}^{-1}$ (1650 ml min⁻¹) of air flow in the cathode, $0.867 \cdot 10^{-5} \text{ m}^3 \text{ s}^{-1}$ (520 ml min⁻¹) of H₂ flow in the anode, and $0.5 \cdot 10^5 \text{ Pa}$ (0.5 bar) of overpressure in the anode and cathode. The RH in anode and cathode is 100%. Cell temperature is set to 80 °C. The stoichiometry for the baseline is $\lambda = 4$ for air and $\lambda = 3$ for H₂. In experiments in which the average current density is varied, airflow stays constant ($2.75 \cdot 10^{-5} \text{ m}^3 \text{ s}^{-1}$ (1650 ml min⁻¹)), the cathode stoichiometry ranges from $\lambda = 20$ for $2 \cdot 10^3 \text{ A m}^{-2}$ (0.2 A cm⁻²) to $\lambda = 2$ for $2 \cdot 10^4 \text{ A m}^{-2}$ (2 A cm⁻²). The cathode stoichiometry, in experiments in which the air flow is varied, average current density stays constant ($1 \cdot 10^4 \text{ A m}^{-2}$ (1 A cm⁻²)), ranges from $\lambda = 4$ for $2.75 \cdot 10^{-5} \text{ m}^3 \text{ s}^{-1}$ (1650 ml min⁻¹) to $\lambda = 1.2$ for $0.833 \cdot 10^{-5} \text{ m}^3 \text{ s}^{-1}$ (500 ml min⁻¹) air flow.

A Höpferl & Hackl electronic load (DS2612) is used to polarize the cell. A National Instruments NI6281 multichannel data acquisition card with 18-bit accuracy is used to obtain the electrochemical noise measurements. The data acquisition card has a sampling frequency of

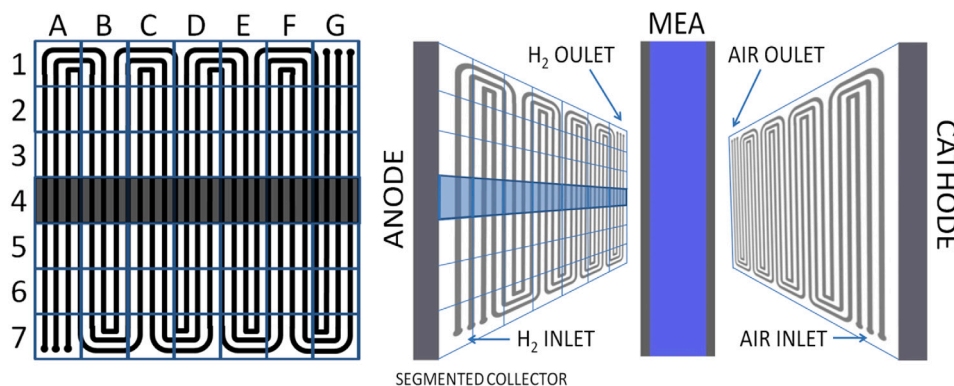


Fig. 1. Scheme of the cell used in the experiments with the 7 segments of local measurement of electrochemical noise (row 4, A–G).

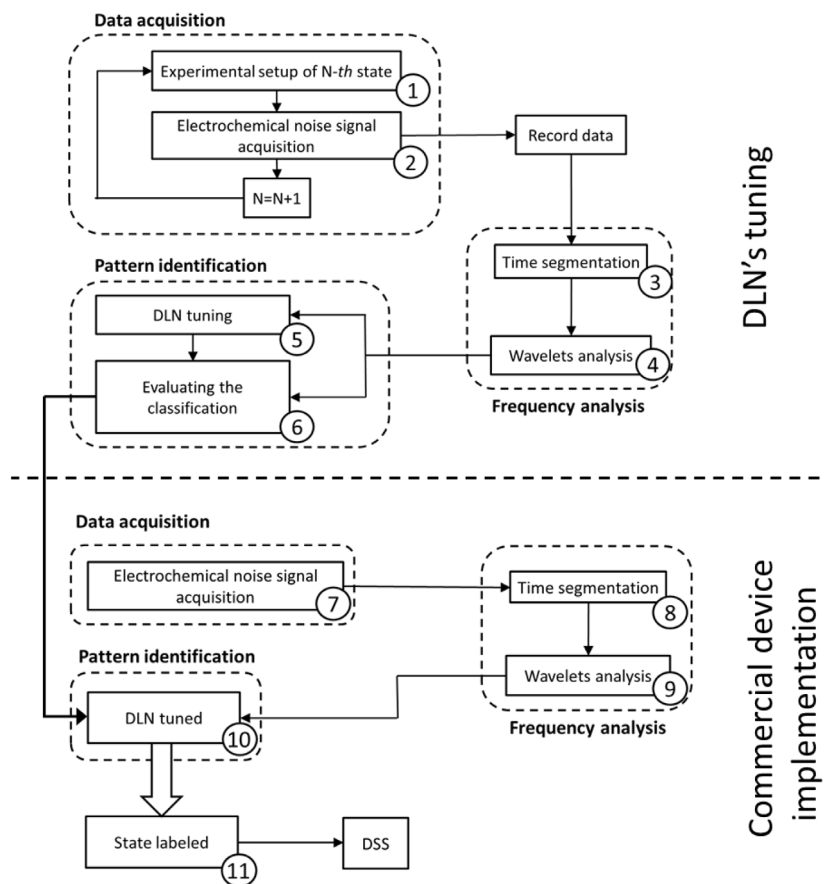


Fig. 2. Scheme of diagnosis procedure.

12800 samples s^{-1} for each of the 7 segments. The signal measurements in the 7 segments are performed simultaneously by the data acquisition card. The oversampling method is applied in the range 1/4, allowing an extra bit of accuracy, obtaining finally 19 bits. The sampling frequency used in the acquisition measurements is 3200 samples s^{-1} , allowing analysis of signals up to 1600 Hz. The precision of the signal in the $\pm 1V$ range is less than $4 \cdot 10^{-6}$ V.

In each of the analyzed states, the EN is measured in the 7 central segments of the cell (see Fig. 1) and, in addition, the current density is measured locally in the 49 cell segments. The 26 experimental states are achieved by varying one factor at a time: 10 different current density values (see Fig. 4a); 5 different airflow values (see Fig. 5a); 10 different cell drying conditions (see Fig. 6a); and 4 different values of the air pressure at the cathode (see Fig. 7a).

The decision of dividing the drying process into 10 states is made because the signal length is long enough to apply the identification procedure explained in the article. Each experiment has a minimum length of 100 s, which allows the acquisition of 50 time-windows of the same state with 2 s length, necessary to carry out the training process and validation of the used neuronal network.

The variation of 4 factors in a series of experiments allows achieving 26 different cell states, whose experimental conditions are described in Table 1.

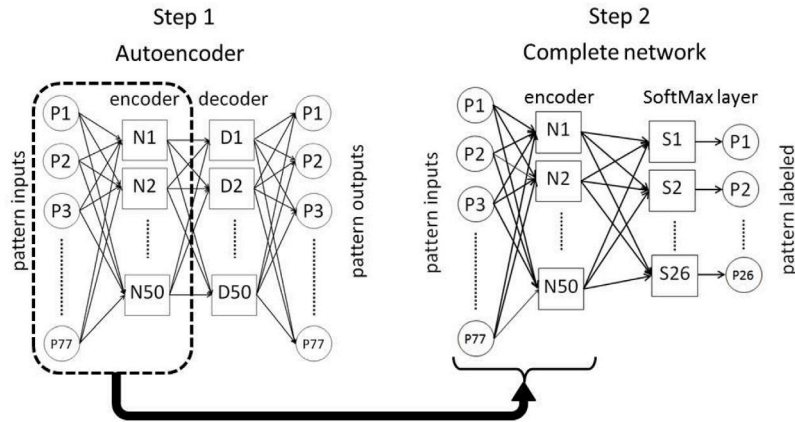
3. Experimental and analysis procedures

To evaluate the capability of the proposed method for the diagnosis of faults and operating states, the experiments described in Table 1 are

Table 1

Experimental configuration of the 26 states to be identified through the method proposed in this work, varying the airflow, the relative cathode gas pressure, the average current density of the cell, and the humidity of gases in anode and cathode, where st. denotes the drying stages during operation at 0% RH., starting from 100% RH.

Experiment #	Av. current $A \cdot m^{-2}$ ($A \cdot cm^{-2}$)	Airflow/Cath. Stoich. $m^3 \cdot s^{-1}$ ($ml \cdot min^{-1}$)/-	Anode-cath. RH %	Rel. cath. pressure Pa (bar)
Ex.1	$0.2 \cdot 10^4$ (0.2)	$2.75 \cdot 10^{-5}$ (1650)/ $\lambda = 20$	100	$0.5 \cdot 10^5$ (0.5)
Ex.2	$0.4 \cdot 10^4$ (0.4)	$2.75 \cdot 10^{-5}$ (1650)/ $\lambda = 10$	100	$0.5 \cdot 10^5$ (0.5)
Ex.3	$0.6 \cdot 10^4$ (0.6)	$2.75 \cdot 10^{-5}$ (1650)/ $\lambda = 6.66$	100	$0.5 \cdot 10^5$ (0.5)
Ex.4	$0.8 \cdot 10^4$ (0.8)	$2.75 \cdot 10^{-5}$ (1650)/ $\lambda = 5$	100	$0.5 \cdot 10^5$ (0.5)
Ex.5 (baseline)	$1 \cdot 10^4$ (1)	$2.75 \cdot 10^{-5}$ (1650)/ $\lambda = 4$	100	$0.5 \cdot 10^5$ (0.5)
Ex.6	$1.2 \cdot 10^4$ (1.2)	$2.75 \cdot 10^{-5}$ (1650)/ $\lambda = 3.33$	100	$0.5 \cdot 10^5$ (0.5)
Ex.7	$1.4 \cdot 10^4$ (1.4)	$2.75 \cdot 10^{-5}$ (1650)/ $\lambda = 2.86$	100	$0.5 \cdot 10^5$ (0.5)
Ex.8	$1.6 \cdot 10^4$ (1.6)	$2.75 \cdot 10^{-5}$ (1650)/ $\lambda = 2.5$	100	$0.5 \cdot 10^5$ (0.5)
Ex.9	$1.8 \cdot 10^4$ (1.8)	$2.75 \cdot 10^{-5}$ (1650)/ $\lambda = 2.22$	100	$0.5 \cdot 10^5$ (0.5)
Ex.10	$2 \cdot 10^4$ (2)	$2.75 \cdot 10^{-5}$ (1650)/ $\lambda = 2$	100	$0.5 \cdot 10^5$ (0.5)
Ex.11	$1 \cdot 10^4$ (1)	$2 \cdot 10^{-5}$ (1200)/ $\lambda = 2.91$	100	$0.5 \cdot 10^5$ (0.5)
Ex.12	$1 \cdot 10^4$ (1)	$1.33 \cdot 10^{-5}$ (800)/ $\lambda = 1.94$	100	$0.5 \cdot 10^5$ (0.5)
Ex.13	$1 \cdot 10^4$ (1)	$1 \cdot 10^{-5}$ (600)/ $\lambda = 1.45$	100	$0.5 \cdot 10^5$ (0.5)
Ex.14	$1 \cdot 10^4$ (1)	$0.83 \cdot 10^{-5}$ (500)/ $\lambda = 1.21$	100	$0.5 \cdot 10^5$ (0.5)
Ex.15	$1 \cdot 10^4$ (1)	$2.75 \cdot 10^{-5}$ (1650)/ $\lambda = 4$	0 (st. 2)	$0.5 \cdot 10^5$ (0.5)
Ex.16	$1 \cdot 10^4$ (1)	$2.75 \cdot 10^{-5}$ (1650)/ $\lambda = 4$	0 (st. 3)	$0.5 \cdot 10^5$ (0.5)
Ex.17	$1 \cdot 10^4$ (1)	$2.75 \cdot 10^{-5}$ (1650)/ $\lambda = 4$	0 (st. 4)	$0.5 \cdot 10^5$ (0.5)
Ex.18	$1 \cdot 10^4$ (1)	$2.75 \cdot 10^{-5}$ (1650)/ $\lambda = 4$	0 (st. 5)	$0.5 \cdot 10^5$ (0.5)
Ex.19	$1 \cdot 10^4$ (1)	$2.75 \cdot 10^{-5}$ (1650)/ $\lambda = 4$	0 (st. 6)	$0.5 \cdot 10^5$ (0.5)
Ex.20	$1 \cdot 10^4$ (1)	$2.75 \cdot 10^{-5}$ (1650)/ $\lambda = 4$	0 (st. 7)	$0.5 \cdot 10^5$ (0.5)
Ex.21	$1 \cdot 10^4$ (1)	$2.75 \cdot 10^{-5}$ (1650)/ $\lambda = 4$	0 (st. 8)	$0.5 \cdot 10^5$ (0.5)
Ex.22	$1 \cdot 10^4$ (1)	$2.75 \cdot 10^{-5}$ (1650)/ $\lambda = 4$	0 (st. 9)	$0.5 \cdot 10^5$ (0.5)
Ex.23	$1 \cdot 10^4$ (1)	$2.75 \cdot 10^{-5}$ (1650)/ $\lambda = 4$	0 (st. 10)	$0.5 \cdot 10^5$ (0.5)
Ex.24	$1 \cdot 10^4$ (1)	$2.75 \cdot 10^{-5}$ (1650)/ $\lambda = 4$	100	$2 \cdot 10^5$ (2)
Ex.25	$1 \cdot 10^4$ (1)	$2.75 \cdot 10^{-5}$ (1650)/ $\lambda = 4$	100	$1 \cdot 10^5$ (1)
Ex.26	$1 \cdot 10^4$ (1)	$2.75 \cdot 10^{-5}$ (1650)/ $\lambda = 4$	100	0 (0)

**Fig. 3.** Autoencoder used in the learning procedure of the deep learning network.

conducted. From each of the states, the characteristic patterns of the EN are obtained. The experimental data are used to perform the tuning of a DLN, evaluating the success of the states' classification. The steps followed to perform the DLN's tuning are described below.

1. Setup of the cell in each of the states to be identified later. In this case, the cell has been setup in 26 states. All states have been achieved out in 4 different types of experiments (current density and airflow variation, cell drying process, and air pressure variation), shown in Section 4.
2. Acquisition of the EN signal in the 7 segments in each of the states. Therefore, 7×26 signals have been acquired, with a length of 100 s.
3. Time segmentation of EN signals. Each of the signals is divided into 2 s time-windows, obtaining 43×7 time-windows for each state. Some time-windows near to the edges of the state were discarded.
4. Analysis in the frequency domain (see Section 3.1) of the EN signals in each time-window and segment, and all states. The

frequency decomposition of the $43 \times 7 \times 26$ signals is performed, obtaining a frequency pattern associated with each segment and for each state. The characteristic pattern of each time-window state is defined by the frequency decomposition of voltage noise in 11 coefficients, each one associated with a frequency.

5. DLN's tuning (see Section 3.2) with the pattern in the frequency domain of each time-window associated with each of the states. All time-window patterns were randomly grouped for NN training (70%), validation (15%), and testing (15%) [52].
6. Evaluation of the NN's capability to classify the states correctly using the tuned DLN.

After evaluating the accuracy of the proposed procedure, the tuned DLN can be implemented in commercial devices, adding a Decision Support System (DSS) for real-time control tasks. This stage, which has not been performed, is described in this work only for the sake of comprehensiveness since the objective is to show the capability of the method for diagnosing operating and fault states using laboratory

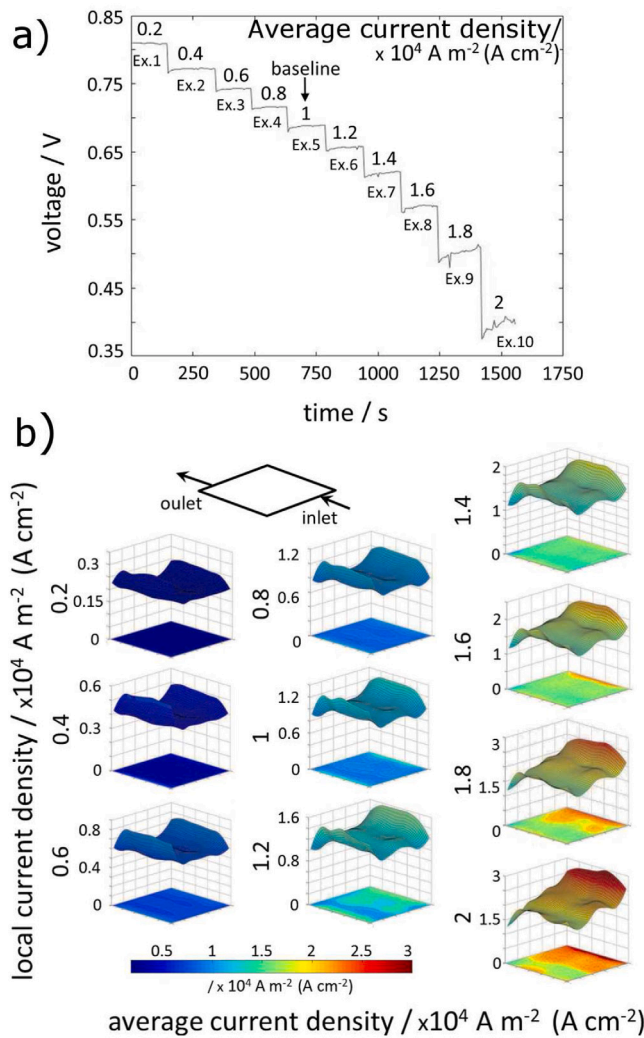


Fig. 4. (a) Cell voltage for different current density values. (b) Local current density for each value of the cell average current density (T_c : 80 °C, relative pressure: $1.5 \cdot 10^5 \text{ Pa}$ (1.5 bar), RH: 100%, H_2 flow: $0.867 \cdot 10^{-5} \text{ m}^3 \text{ s}^{-1}$ (520 ml min^{-1}), airflow: $2.75 \cdot 10^{-5} \text{ m}^3 \text{ s}^{-1}$ (1650 ml min^{-1})).

equipment. The steps of the procedure for the implementation of the method in commercial devices are described below.

7. Acquisition of the cell EN signal in operation from the 7 cell segments, using the same card acquisition configuration as in the DLN's tuning stage.
8. Time segmentation of noise signals in time-windows.
9. Frequency domain analysis of the EN signals in each time-window and each segment using real-time WT.
10. Input the pattern compound with the WT coefficients (with the identical format of the tuning stage), obtaining from the tuned DLN the cell's labeled state.
11. Finally, use the obtained labeled state in a Decision Support System (DSS) to get a recommended action (e.g., warning alarm or stop operation).

The steps that compose the DLN's tuning, and the commercial device implementation procedures are shown schematically in Fig. 2.

3.1. Frequency analysis

In order to obtain a characteristic pattern of each state, the noise signal of each of the 7 segments is analyzed in the frequency domain. The

characteristic pattern is composed of discrete frequency coefficients, which are calculated using a continuous wavelet transform (CWT). The CWT has been performed using the Wavelet Transform Matlab's toolbox [53]. The efficacy of obtaining the frequency patterns of EN using CWT compared with Fast Fourier Transform has been studied in [48], getting similar results. The use of WT is preferred in our method, because WT is better suited for real-time applications. The CWT has demonstrated great effectiveness in characterizing the frequencies of the electrochemical noise signals [48]. The transformed wavelet Gauss type 4, which has the shape of Eq. (1), was used in this study. It showed similar results compared with other functions such as Haar, Mexican Hat, or Daubechies [48]. The coefficient C_4 must satisfy the 2-norm of $\psi_{\text{Gauss}}(t)$ equals one.

$$\psi_{\text{Gauss}}(t) = C_4 \frac{d^4}{dt^4} (e^{-t^2}) \quad (1)$$

The following 11 frequency values have been selected: 0.1, 0.2, 0.5, 1.5, 3, 7, 16, 37, 70, 120, and 200 Hz. These values have approximately a logarithmic relationship in the 0.1–200 Hz range. The CWT coefficients, W , are calculated using Eq. (2), where a is the scale factor, ψ^* is the complex conjugate of the wavelet function, and b is the shift factor.

$$W(a, b, f(t), \psi(t)) = \int_{-\infty}^{\infty} f(t) \frac{1}{\sqrt{a}} \psi^* \left(\frac{t-b}{a} \right) dt \quad (2)$$

The scaling factor a of the Gaussian function type 4, for the frequencies under study f_a (i.e., 0.1, 0.2, 0.5, 1.5, 3, 7, 16, 37, 70, 120, and 200 Hz), depends on the measurement sampling period $T_s = 3.125 \cdot 10^{-4} \text{ s}$ and the characteristic coefficient of the function $f_c = 0.5$. It is calculated from Eq. (3).

$$a = \frac{f_c}{f_a T_s} \quad (3)$$

The following 11 scale factors are obtained: 16 000, 8000, 3200, 1067, 533, 229, 100, 43, 23, 13 and 8. To calculate the characteristic value associated with that frequency, the standard deviation associated to the m th coefficient for that frequency in the time-window is calculated as shown in Eq. (4),

$$\sigma_W(m, N) = \sqrt{\frac{\sum_{n=1}^N (W(m, n) - \bar{W}(m, N))^2}{N-1}} \quad (4)$$

where N is the total number of samples of the time-window, and the average value of the wavelet coefficient, $\bar{W}(m, N)$, is calculated from Eq. (5).

$$\bar{W}(m, N) = \frac{1}{N} \sum_{n=1}^N W(m, n) \quad (5)$$

The use of a large number of frequencies through the decomposition with the CWT of EN signal, allows a more detailed analysis of the frequency range, since the gap between the selected frequencies is reduced. The study of a large number of frequencies is possible due to DLNs eliminate non-relevant information without producing a negative effect on the accuracy of the states' classification. The use of 11 frequencies balances the computational effort of the identification procedure and the accuracy of the input DLN's pattern.

3.2. Deep learning classification

As described at the beginning of this section, artificial DLN is used to identify the states produced by the variation of the cell operating parameters. The artificial DLN developed in this work is compound by two networks that must be tuned separately but sequentially. Firstly, the codification of the patterns is carried out by autoencoders. The autoencoders are networks that allow extracting useful information from large volumes of sparse information [54]. The autoencoders are NN of unsupervised learning, with a structure formed by an encoder and a

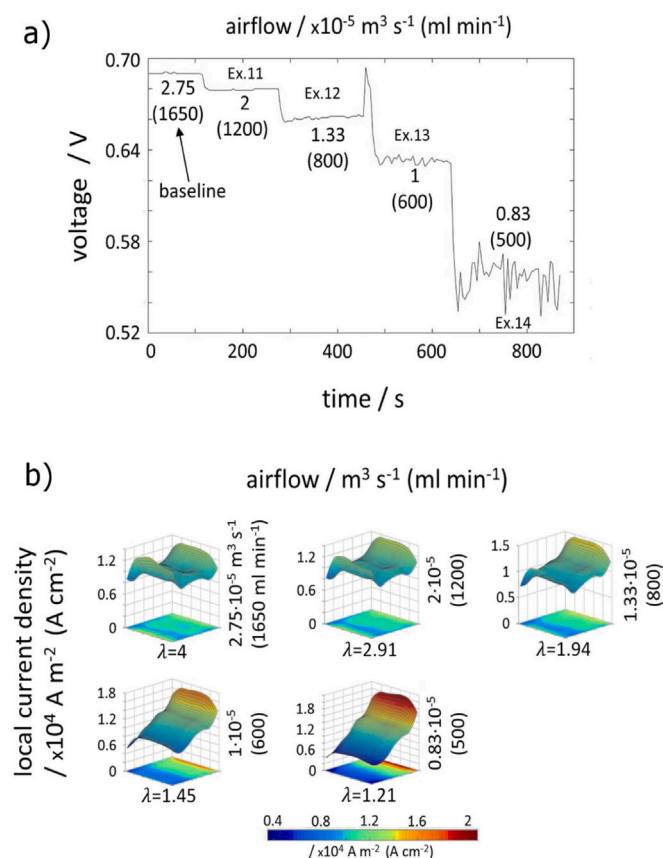


Fig. 5. (a) Cell voltage for different airflow values. (b) Local current density for each cell airflow value and stoichiometry (T_c : 80 °C, average current density ($1 \cdot 10^4 \text{ A m}^{-2}$ (1 A cm^{-2})), relative pressure: $1.5 \cdot 10^5 \text{ Pa}$ (1.5 bar), RH: 100%, H_2 flow: $0.867 \cdot 10^{-5} \text{ m}^3 \text{ s}^{-1}$ (520 ml min $^{-1}$)).

decoder as shown schematically in Step 1 of Fig. 3. The output does not need to be labeled, using the same input pattern. An exhaustive search of the optimal number of nodes of the autoencoder hidden layer has been carried out, obtaining the best results with 50 nodes.

After the autoencoder has been tuned, the encoder part is connected to a SoftMax network as the last classification layer; in this stage, the complete network is tuned with the class labeled in Step 2, Fig. 3. The applied NN structure is commonly used in DLNs for classification purposes [55–57]. The DLN has been implemented with the Deep Learning Matlab toolbox [52]. The state or failure identification procedure has two stages, corresponding to the pattern classification process of the NN: (a) a tuning stage, which requires the previous classification of a significant number of EN patterns related to each state; and (b) the use of the tuned NN to identify the states. In this case, to evaluate the reliability of the used NN setup, the use of conventional NN for identification purposes has been analyzed in both cases, and similar results have been obtained. The use of the DLN versus conventional NN is due to the DLN's capability to handle more input variables of the pattern if necessary, so it is considered a better classification method.

In addition, improvement in the success rate identification has been evaluated by adding to the frequency coefficients of the electrochemical noise the measurement of the average cell voltage at the DLN's input.

Due to the similarity between some of the states, especially those produced by varying the current density and the cell's drying process, this work analyzes the impact of reducing the number of states on the successful identification of these states. This analysis is conducted by incorporating the success rate of the adjacent states in the success rate in identifying a state.

States that are consecutive and do not belong to the same type of experiment will not be considered to calculate the classification success rate.

4. Experimental results

The PEMFC performance strongly depends on the operating conditions. Thereby, local performance varies by changing the global operating conditions and the flow field of the cell. Moreover, various operating parameters such as average current density, relative humidity (RH), gas concentration, and cathode pressure influence the current density's homogeneity.

This work shows experimental validation of the proposed method's capability, as an in-situ diagnostic tool, to identify failures in PEMFC. The experiments were designed to determine how the EN analysis can locally detect and diagnose states related to a non-homogeneous condition such as RH, gas concentration, and drop in the air pressure.

The voltage in each state of the airflow and cathode pressure experiments (see Figs. 4a, 5a and 7a) maintains a quasi-stationary value. In contrast, in the dehydration experiment (see Fig. 6a), the cell shows a progressive voltage drop over time.

4.1. Average current density

This experimental setup considers 10 different values of average current density. The polarized cell for current density has been applied in increasing values, as shown in Fig. 4a. The average current density was held for each value during a similar time (100 s). Fig. 4a shows that a quasi-stationary voltage is reached only for low current densities ($< 1.2 \cdot 10^4 \text{ A m}^{-2}$ (1.2 A cm^{-2})), due to the flow field and mass transport issues at high currents. The effect of overshoot on the voltage due to current steps has been studied in [58,59]. Fig. 4b shows the spatial current density distribution for each cell average current density value shown in Fig. 4a. In Fig. 4b, the significant gradient of the spatial current density is only observed for the highest average current density values ($> 1 \cdot 10^4 \text{ A m}^{-2}$ (1 A cm^{-2})), due to the gradual shortage of gas concentration close to the gas outlets. Heterogeneity in the local current density distribution has been observed in other studies under different operating conditions [14,60–63].

4.2. Airflow

The influence of a drastic reduction of the airflow is evaluated. The cathode side flow is diminished from the baseline conditions ($2.75 \cdot 10^{-5} \text{ m}^3 \text{ s}^{-1}$ (1650 ml min $^{-1}$)) until $0.83 \cdot 10^{-5} \text{ m}^3 \text{ s}^{-1}$ (500 ml min $^{-1}$) in 5 steps. In this experiment, the airflow is kept constant. Therefore, when the average current density of the cell is modified, the stoichiometry of the cathode is also modified (from 1650 ml min $^{-1}$, $\lambda = 4$ to 500 ml min $^{-1}$, $\lambda = 1.21$). In the case of high currents, a low overstoichiometric ratio is achieved, producing a starvation phenomenon.

Fig. 5a shows the cell voltage for different airflow values (5 states), and Fig. 5b shows the spatial current density related to these states. Although the voltage differences between states, produced as a consequence of reducing the airflows, are small (max. 0.150 V), the oxygen starvation conditions drag the cell into a non-homogeneous current distribution, correlated with a non-stable voltage response, as shown in Fig. 5a. As is expected, under conditions of low air stoichiometry, the higher values of the current are located at the inlet of the gases, where oxygen stoichiometry remains higher.

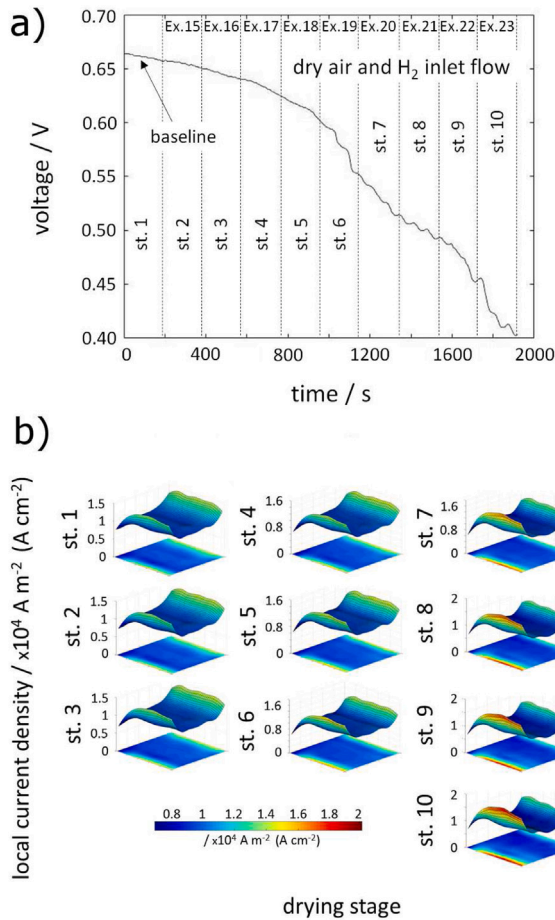


Fig. 6. (a) Time evolution of the voltage due to dry gases in the cell. (b) Local current density for the selected drying stages of the cell (T_c : 80 °C, average current density: $1 \cdot 10^4 \text{ A m}^{-2}$ (1 A cm^{-2}), RH: 100%, H_2 relative pressure: $1.5 \cdot 10^5 \text{ Pa}$ (1.5 bar), H_2 flow: $0.867 \cdot 10^{-5} \text{ m}^3 \text{ s}^{-1}$ (520 ml min^{-1}), airflow: $2.75 \cdot 10^{-5} \text{ m}^3 \text{ s}^{-1}$ (1650 ml min^{-1})).

4.3. Dry gases

The effect of feeding the cell with dry gases (non-humidified) is studied. Fig. 6a shows the time evolution of the voltage drop induced by the cell drying when dry gases are used [64,65], starting from the baseline setup, steady-state condition, where high humidity gases (RH 100%) are used. The time origin is set at the instant when the bubbler's bypass is switched on, and the humidity of the inlet gases changed to non-humidified in both electrodes. Fig. 6b shows the local current distribution in each of the 10 states of cell drying. The cell voltage falls significantly in the drying process after 2000 s; the voltage drop is related to the active area reduction as the cell becomes dehydrated. This phenomenon is dominant when the cell voltage drops to low voltage values (under 0.4 V) [62]. In order to avoid irreversible degradation, lower values of the voltage are not explored in this work.

4.4. Air pressure

In the last experiments, 4 different cell states are achieved as a result of varying the air relative pressure value from $2 \cdot 10^5 \text{ Pa}$ (2 bar) up to 0 Pa ($3 \cdot 10^5 \text{ Pa}$ (3 bar) to $1 \cdot 10^5 \text{ Pa}$ (1 bar) of absolute pressure). Fig. 7a shows the cell voltage for different pressure values at the cathode, and Fig. 7b shows the local current density corresponding to each of these values. The air pressure variation at the cathode produces a relatively small voltage drop ($\approx 0.1 \text{ V}$), and there are no significant differences in the spatial distribution of current density.

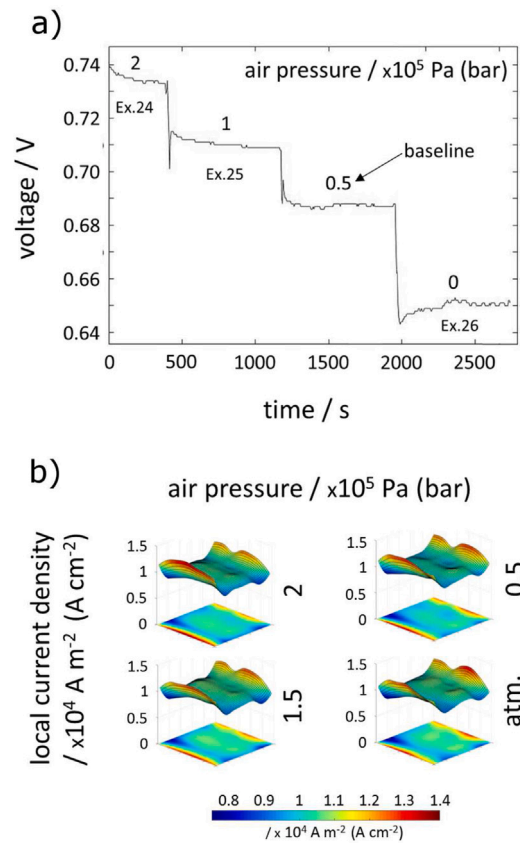


Fig. 7. (a) Cell voltage for different air pressure values. (b) Local current density for each value of the air pressure (T_c : 80 °C, average current density: $1 \cdot 10^4 \text{ A m}^{-2}$ (1 A cm^{-2}), RH: 100%, H_2 relative pressure: $1.5 \cdot 10^5 \text{ Pa}$ (1.5 bar), H_2 flow: $0.867 \cdot 10^{-5} \text{ m}^3 \text{ s}^{-1}$ (520 ml min^{-1}), airflow: $2.75 \cdot 10^{-5} \text{ m}^3 \text{ s}^{-1}$ (1650 ml min^{-1})).

5. State identification results

The classification method proposed in this work has been used to identify operating states, many of which are very close to the nominal operating conditions of the cell, so that they could not be considered operating failures. This feature makes the classification process more complicated, since the differences between states may be small.

In the classification process, two configurations of DLN inputs have been evaluated. On the one hand, only EN patterns have been used. On the other hand, EN patterns have been used together with the average cell voltage of the state, in order to improve the classification success. Fig. 8a shows the confusion matrix for classification with and without using the cell's average voltage. The confusion matrix represents the classification's successful results, where the y-axis shows the states to be classified, and the x-axis indicates the classified states. Therefore, the sum of the classification rate of each state along the x-axis is 1. In the confusion matrix, the diagonal shows the state classification's success rate, where the value 1 on the diagonal indicates that the state has been correctly identified with a 100% success.

The use of the cell voltage produces a significant improvement in the states' successful classification, as is observed in Fig. 8a. The classification error is produced mainly in contiguous states, as shown in Fig. 8a.

If the voltage is not taken into account, the classification's average success rate is 66.06%, and it is 86.45% if the classification is performed considering the cell's voltage. The successful classification rate of the immediately contiguous states is added to the rate of each state, due to the experimental configuration and the proximity of the operating points between the contiguous states.

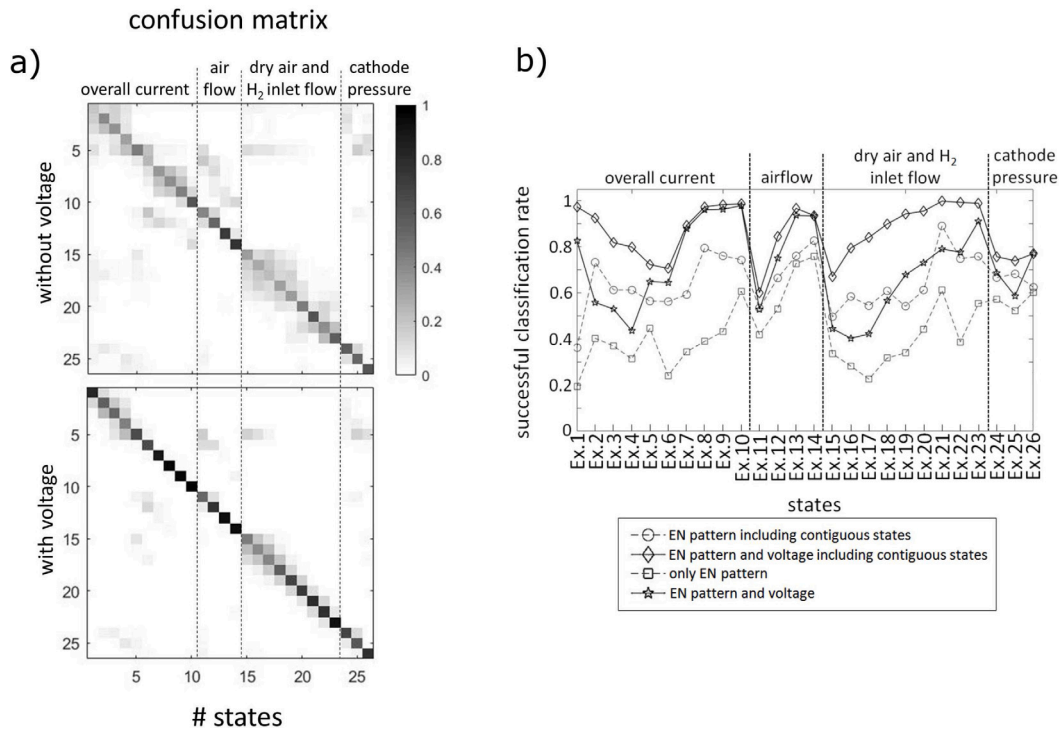


Fig. 8. (a) Confusion matrix of the operating state classifications with and without considering the average cell voltage. (b) Rate of successful classification, including or not the average cell voltage in the DLN input, and taking into account or not the classification errors of the contiguous states.

If the contiguous states are considered, the classification success of the state is added to the classification error of the immediately contiguous states, in order to calculate the classification success rate of the state (i.e., the classification success rate of state #5 is the sum of the classification rate of state #5 plus the error classification rates of states #4 and #6, when the EN patterns corresponding to state #5 have been used to classify the state #5). The pairs (#10, #11), (#14, #15), and (#23, #24) were not considered contiguous states to calculate the success rate since these states do not belong to the same group of experiments.

Fig. 8b shows the success rate values calculated in the 4 following ways:

- Without taking into account the cell voltage and without considering the success classification of the contiguous states.
- Taking into account the cell voltage, but without considering the contiguous states.
- Without taking into account the cell voltage and considering the contiguous states.
- Taking into account the cell voltage and considering contiguous states.

The states that show a behavior farther away from the nominal operating conditions obtain a higher success rate, close to 90%. The rate is lower in the case of the different cathode pressure values, which do not show a substantial change in the performance of the cell, which is evidenced by a small effect on the over-voltage and a small variation in the local current distribution.

6. Conclusions

This paper describes a novel methodology for diagnosing malfunctions using EN locally (i.e., EN measured in different parts of the cell at the same time). The use of the EN signals of 7 different sites in the cell simultaneously allows the information from the signals to represent the non-homogeneity behavior of the cell, thus improving the identification capability of this method. In addition, the frequency analysis of the EN

signals is performed using WT, which allows obtaining a characteristic pattern of each state to identify. The use of Deep Learning Networks allows the identification of 26 different states, produced by the variation of the average current density, the airflow, the drying process, and air pressure. The number of states to be identified in this paper is the largest performed in previous studies on PEMFC diagnosis. The mean successful identification rate of the 26 states is 86.45% considering the contiguous states. The use of this method can be extended to other phenomena such as failure modes or operation setup. The described method is non-intrusive and allows the diagnosis of malfunctions with the cell in operation, i.e. without stopping it. Moreover, the method can be implemented in unexpensive and lightweight commercial systems. The diagnosis of the states allows control decisions to be adopted to improve the robustness of the cell and the durability of the components since early diagnosis will allow, for example, to anticipate irreversible damages in the cell. In future work, the capability to extrapolate the described method to fuel cells with different physical configurations should be evaluated since the success of state identification could be decreased. If this is confirmed, the DLN should be tuned for each cell configuration.

List of acronyms

- cFRA** Co-alternating frequency response analysis
- CWT** Continuous wavelet transform
- DLN** Deep learning network
- DSS** Decision support system
- EIS** Electrochemical impedance spectroscopy
- EN** Electrochemical noise
- GDL** Gas diffusion layer
- NN** Neural network

PCB Printed circuit board

PEMFC Proton exchange membrane fuel cell

RH Relative humidity

SVM Support vector machine

WT Wavelet transform

CRediT authorship contribution statement

M.A. Rubio: Formal analysis, Validation, Software, Methodology, Conceptualization, Investigation, Writing – original draft, Visualization, Writing – review & editing. **D.G. Sanchez:** Validation, Software, Methodology, Conceptualization, Investigation, Writing – original draft, Visualization, Writing – review & editing. **P. Gazdzicki:** Investigation, Supervision, Writing – review & editing. **K.A. Friedrich:** Methodology, Investigation, Supervision, Writing – review & editing. **A. Urquía:** Methodology, Conceptualization, Investigation, Funding acquisition, Project administration, Supervision, Writing – review & editing.

Declaration of competing interest

The authors declare that they have no known competing financial interests or personal relationships that could have appeared to influence the work reported in this paper.

Acknowledgments

Work performed by Miguel Angel Rubio and Alfonso Urquía was supported by the Ministerio de Economía y Competitividad of Spain (DPI2013-42941-R grant) and the Research Promotion Plan of UNED, Spain.

References

- [1] J. Wang, System integration, durability and reliability of fuel cells: Challenges and solutions, *Appl. Energy* 189 (2017) 460–479.
- [2] E. Pahon, S. Jemei, D. Hissel, Supervised classification approach dedicated to proton exchange membrane fuel cell diagnostic, in: *IEEE 12th International Symposium on Diagnostics for Electrical Machines, Power Electronics and Drives*, 2019, pp. 446–451.
- [3] C. Gabrielli, B. Tribollet, A transfer function approach for a generalized electrochemical impedance spectroscopy, *J. Electrochem. Soc.* 141 (1994) 1147–1157.
- [4] F. Knorr, D. Garcia-Sanchez, J. Schirmer, P. Gazdzicki, K.A. Friedrich, Methanol as antifreeze agent for cold start of automotive polymer electrolyte membrane fuel cells, *Appl. Energy* 238 (2019) 1–10.
- [5] M.A. Rubio, A. Urquía, S. Dormido, Diagnosis of performance degradation phenomena in PEM fuel cells, *Int. J. Hydrog. Energy* 35 (2010) 2586–2590.
- [6] L. Russo, M. Sorrentino, P. Polverino, C. Pianese, Application of buckingham Pi theorem for scaling-up oriented fast modelling of proton exchange membrane fuel cell impedance, *J. Power Sources* 353 (2017) 277–286.
- [7] P. Polverino, G. Bove, M. Sorrentino, C. Pianese, D. Beretta, Advancements on scaling-up simulation of proton exchange membrane fuel cells impedance through buckingham Pi theorem, *Appl. Energy* 249 (2019) 245–252.
- [8] M.A. Rubio, A. Urquía, S. Dormido, Diagnosis of PEM fuel cells through current interruption, *J. Power Sources* 171 (2007) 670–677.
- [9] T. Mennola, M. Mikkola, M. Noponen, T. Hottinen, P. Lund, Measurement of ohmic voltage losses in individual cells of a PEMFC stack, *J. Power Sources* 112 (2002) 261–272.
- [10] N. Rajalakshmi, M. Raja, K.S. Dhathathreyan, Evaluation of current distribution in a proton exchange membrane fuel cell by segmented cell approach, *J. Power Sources* 112 (2002) 331–336.
- [11] T.V. Reshetenko, K. Bethune, M.A. Rubio, J. St-Pierre, Study of low concentration CO poisoning of Pt anode in a protonexchange membrane fuel cell using spatial electrochemical impedancespectroscopy, *J. Power Sources* 269 (2014) 344–362.
- [12] T.V. Reshetenko, J. St-Pierre, Study of acetylene poisoning of Pt cathode on proton exchange membrane fuel cell spatial performance using a segmented cell system, *J. Power Sources* 287 (2015) 401–415.
- [13] M. Schulze, E. Gülzow, St. Schönbauer, T. Knöri, R. Reissner, Segmented cells as tool for development of fuel cells and error prevention/prediagnostic in fuel cell stacks, *J. Power Sources* 173 (2007) 19–27.
- [14] D. Garcia-Sanchez, T. Morawietz, P. Gama da Rocha, R. Hiesgen, P. Gazdzicki, K.A. Friedrich, Local impact of load cycling on degradation in polymer electrolyte fuel cells, *Appl. Energy* 259 (2020) 114210.
- [15] A.M. Niroumand, W. Merida, M. Eikerling, M. Safi, Pressure voltage oscillations as diagnostic tool for PEFC cathode, *Electrochem. Commun.* 12 (2010) 122–124.
- [16] A. Sorrentino, T. Vidakovic-Koch, K. Sundmacher, Studying mass transport dynamics in polymer electrolyte membrane fuel cells using concentration-alternating frequency response analysis, *J. Power Sources* 412 (2019) 331–335.
- [17] Z. Hu, L. Xu, Y. Huang, J. Li, M. Ouyang, X. Du, H. Jiang, Comprehensive analysis of galvanostatic charge method for fuel cell degradation diagnosis, *Appl. Energy* 212 (2019) 1321–1332.
- [18] M. Bressel, M. Hilaret, D. Hissel, B.O. Bouamama, Extended Kalman filter for prognostic of proton exchange membrane fuel cell, *Appl. Energy* 164 (2016) 220–227.
- [19] Z. Li, R. Outbib, S. Giurgea, D. Hissel, S. Jemei, A. Giraud, S. Rosini, Online implementation of SVM based fault diagnosis strategy for PEMFC systems, *Appl. Energy* 164 (2016) 284–293.
- [20] Z. Li, R. Outbib, S. Giurgea, D. Hissel, S. Jemei, A. Giraud, P. Couderc, Fault diagnosis for fuel cell systems: A data-driven approach using high-precision voltage sensors, *Renew. Energy* 135 (2019) 1435–1444.
- [21] D. Benouioua, D. Candusso, F. Harel, L. Oukhellou, PEMFC stack voltage singularity measurement and fault classification, *Int. J. Hydrog. Energy* 39 (2014) 21631–21637.
- [22] H. Liu, J. Chen, D. Hissel, H. Su, Remaining useful life estimation for proton exchange membrane fuel cells using a hybrid method, *Appl. Energy* 249 (2019) 910–919.
- [23] X. Wu, B. Zhou, Fault tolerance control for proton exchange membrane fuel cell systems, *J. Power Sources* 324 (2016) 804–829.
- [24] P. Polverino, E. Frisk, D. Jung, M. Krysanter, C. Pianese, Model-based diagnosis through structural analysis and causal computation for automotive polymer electrolyte membrane fuel cell systems, *J. Power Sources* 357 (2017) 26–40.
- [25] Z. Zehan, L. Shuanghong, X. Yawen, Y. Yupu, Intelligent simultaneous fault diagnosis for solid oxide fuel cell system based on deep learning, *Appl. Energy* 233–234 (2019) 930–942.
- [26] X. Wang, J. Chen, S. Quan, Y.-X. Wang, H. He, Hierarchical model predictive control via deep learning vehicle speed predictions for oxygen stoichiometry regulation of fuel cells, *Appl. Energy* 276 (2020) 115460.
- [27] P.C. Searson, J.L. Dawson, Analysis of electrochemical noise generated by corroding electrodes under open-circuit conditions, *J. Electrochem. Soc.* 135 (1988) 1908–1915.
- [28] C. Gabrielli, M. Keddam, Review of applications of impedance and noise analysis to uniform and localized corrosion, *Corrosion* 48 (1992) 794–811.
- [29] A. Legat, V. Dolecek, Corrosion monitoring system based on measurement and analysis of electrochemical noise, *Corrosion* 51 (1995) 295–300.
- [30] D.-H. Xia, S. Song, Y. Behnamian, W. Hu, Y.F. Cheng, J.-L. Luo, F. Huet, Review - electrochemical noise applied in corrosion science: theoretical and mathematical models towards quantitative analysis, *J. Electrochem. Soc.* 167 (2020) 1908–1915.
- [31] H. Xiao, F. Mansfeld, Evaluation of coating degradation with electrochemical impedance spectroscopy and electrochemical noise analysis, *J. Electrochem. Soc.* 141 (1994) 2332–2337.
- [32] F. Mansfeld, C.C. Lee, G. Zhang, Comparison of electrochemical impedance and noise data in frequency domain, *Electrochim. Acta* 43 (1998) 435–438.
- [33] H. Greisiger, T. Schauer, On the interpretation of the electrochemical noise data for coating, *Prog. Org. Coat.* 39 (2000) 31–36.
- [34] P.R. Roberge, R. Beaudoin, Voltage noise measurements on sealed lead-acid batteries, *J. Power Sources* 27 (1989) 177–186.
- [35] S. Martinet, R. Durand, P. Ozil, P. Leblanc, P. Blanchard, Application of electrochemical noise analysis to the study of batteries: state-of-charge determination and overcharge detection, *J. Power Sources* 83 (1999) 83–93.
- [36] D.H.J. Baert, A.A.K. Vervae, Small bandwidth measurement of the noise voltage of batteries, *J. Power Sources* 114 (2003) 357–365.
- [37] S. Martemianov, N. Adiutantov, Y.K. Evdokimov, L. Madier, F. Maillard, A. Thomas, New methodology of electrochemical system analysis and applications for commercial Li-ion batteries, *J. Solid State Electrochem.* 19 (2015) 2803–2810.
- [38] Y. Tan, Q. Xie, J. Huang, W. Duan, M. Ma, S. Yao, Study on glucose biofuel cells using an electrochemical noise device, *Electroanalysis* 20 (2008) 1599–1606.
- [39] S. Giurgea, R. Timovan, D. Hissel, R. Outbib, An analysis of fluidic voltage statistical correlation for a diagnosis of PEM fuel cell flooding, *Int. J. Hydrog. Energy* 38 (2013) 4689–4696.
- [40] K.T. Koshekov, Y.N. Klikushin, V.Y. Kobenko, Y.K. Evdokimov, A.V. Demyanenko, Fuel cell diagnostics using identification measurement theory, *J. Fuel Cell Sci. Technol.* 11 (2014) 051003.
- [41] E.A. Astafiev, A. Ukshe, E. Gerasimova, R. Manzhos, Electrochemical noise of a hydrogen-air polymer electrolyte fuel cell operating at different loads, *J. Solid State Electrochem.* 22 (2018) 1839–1849.

- [42] G. Gabrielli, F. Huet, M. Keddam, Fluctuations in electrochemical systems. I. General theory on diffusion limited electrochemical reactions, *J. Chem. Phys.* 99 (1993) 7232–7239.
- [43] G. Gabrielli, F. Huet, M. Keddam, Fluctuations in electrochemical systems. II. Application to a diffusion limited redox process, *J. Chem. Phys.* 99 (1993) 7240–7252.
- [44] E.A. Astafiev, Electrochemical noise measurement of polymer membrane fuel cell under load, *Russ. J. Electrochem.* 54 (2018) 554–560.
- [45] B. Legros, P.-X. Thivel, Y. Bultel, R.P. Nogueira, First results on PEMFC diagnosis by electrochemical noise, *Electrochem. Commun.* 13 (2011) 1514–1516.
- [46] S. Giurgea, R. Tirnovan, D. Hissel, R. Outbib, An analysis of fluidic voltage statistical correlation for a diagnosis of PEM fuel cell flooding, *Int. J. Hydrog. Energy* 38 (2013) 4689–4696.
- [47] E. Pahon, N.Y. Steiner, S. Jemei, D. Hissel, P. Mocoteguy, A signal-based method for fast PEMFC diagnosis, *Appl. Energy* 165 (2016) 748–758.
- [48] M.A. Rubio, K. Bethune, A. Urquia, J. St-Pierre, Proton exchange membrane fuel cell failure mode early diagnosis with wavelet analysis of electrochemical noise, *Int. J. Hydrog. Energy* 41 (2016) 14991–15001.
- [49] K. Javed, R. Gouriveau, N. Zerhouni, D. Hissel, Prognostics of proton exchange membrane fuel cells stack using an ensemble of constraints based connectionist networks, *J. Power Sources* 324 (2016) 745–757.
- [50] T. Kaz, H. Sander, Device for measuring local current/heat distribution on electrochemical electrode has current flow direction to resistance element transverse to current flow direction to current conducting element, 2004, German Patent DE10316117 B3.
- [51] T. Kaz, H. Sander, Measurement of the current distribution/heat distribution of an electrochemical electrode, 2006, Global Patent Index EP1618395 A1.
- [52] Mathworks documentation, Deep Learning Toolbox, Mathworks, URL <https://www.mathworks.com/help/deeplearning>.
- [53] Mathworks documentation, Wavelets Toolbox, Mathworks, URL <https://www.mathworks.com/help/wavelet>.
- [54] A. Shrestha, A. Mahmood, Review of deep learning algorithms and architectures, *IEEE Access* 7 (2019) 53040–53065.
- [55] H.I. Fawaz, G. Forestier, J. Weber, L. Idoumghar, P. Muller, Deep learning for time series classification: a review, *Data Min. Knowl. Discov.* 33 (2019) 917–963.
- [56] Y. Zheng, T. Wang, B. Xin, T. Xie, Y. Wang, Sparse autoencoder and softmax regression based diagnosis method for the attachment on the blades of marine current turbine, *Sensors* 19 (2019) 826.
- [57] M.M. Al Rahhal, Y. Bazi, H. AlHichri, N. Alajlan, F. Melgani, R.R. Yager, Deep learning approach for active classification of electrocardiogram signals, *Inform. Sci.* 345 (2016) 340–354.
- [58] Z. Huang, J. Shen, S.H. Chan, Z. Tu, Transient response of performance in a proton exchange membrane fuel cell under dynamic loading, *Energy Convers. Manage.* 226 (2020) 113492.
- [59] L. Zhao, J. Brouwer, S. James, J. Siegler, E. Peterson, A. Kansal, J. Liu, Dynamic performance of an in-rack proton exchange membrane fuel cell battery system to power servers, *Int. J. Hydrog. Energy* 42 (2017) 10158–10174.
- [60] D.G. Sanchez, D. Guinea, R. Hiesgen, I. Wehl, K.A. Friedrich, Oscillations of PEM fuel cells at low cathode humidification, *J. Electroanal. Chem.* 649 (2010) 219–231.
- [61] D.G. Sanchez, P.L. Garcia-Ybarra, PEMFC operation failure under severe dehydration, *Int. J. Hydrog. Energy* 37 (2012) 7279–7288.
- [62] D. Garcia-Sanchez, T. Ruiju, K.A. Friedrich, J. Sanchez-Monreal, M. Vera, Analysis of the influence of temperature and gas humidity on the performance stability of polymer electrolyte membrane fuel cells, *J. Electrochem. Soc.* 163 (2016) F150–F159.
- [63] J.J. Hwnag, W.R. Chang, R.G. Peng, P.Y. Chen, A. Su, Experimental and numerical studies of local current mapping on a PEM fuel cell, *Int. J. Hydrog. Energy* 33 (2008) 5718–5727.
- [64] D. Garcia-Sanchez, T. Ruiju, I. Biswas, K.A. Friedrich, J. Sanchez-Monreal, M. Vera, Effect of the inlet gas humidification on PEMFC behavior and current density distribution, *ECS Trans.* 64 (2014) 603–617.
- [65] D. Cha, W. Yang, Y. Kim, Performance improvement of self-humidifying PEM fuel cells using water injection at various start-up conditions, *Energy* 183 (2019) 514–524.